
















AN INTERMEDIATE MASS BLACK HOLE HIDDEN BEHIND THICK OBSCURATION

PETER G. BOORMAN ¹, DANIEL STERN ², ROBERTO J. ASSEF ³, ABHIJEET BORKAR ⁴, MURRAY BRIGHTMAN ¹,
JOHANNES BUCHNER ^{5,6}, CHIEN-TING CHEN ^{7,8}, HANNAH P. EARNSHAW ¹, FIONA A. HARRISON ¹,
GABRIELE A. MATZEU ⁹, RYAN W. PFEIFLE ^{10,11,*}, CLAUDIO RICCI ^{3,12}, JIŘÍ SVOBODA ⁴,
NÚRIA TORRES-ALBÀ ^{13,14,†} AND INGYIN ZAW ¹⁵

¹*Cahill Center for Astrophysics, California Institute of Technology, 1216 East California Boulevard, Pasadena, CA 91125, USA*

²*Jet Propulsion Laboratory, California Institute of Technology, Pasadena, CA 91109, USA*

³*Instituto de Estudios Astrofísicos, Facultad de Ingeniería y Ciencias, Universidad Diego Portales, Av. Ejército Libertador 441, Santiago, Chile*

⁴*Astronomical Institute, Academy of Sciences, Boční II 1401, CZ-14131 Prague, Czech Republic*

⁵*Max Planck Institute for Extraterrestrial Physics, Giessenbachstrasse, 85741 Garching, Germany*

⁶*Excellence Cluster Universe, Boltzmannstr. 2, D-85748, Garching, Germany*

⁷*Science and Technology Institute, Universities Space Research Association, Huntsville, AL 35805, USA*

⁸*Astrophysics Office, NASA Marshall Space Flight Center, ST12, Huntsville, AL 35812, USA*

⁹*Quasar Science Resources SL for ESA, European Space Astronomy Centre (ESAC), Science Operations Department, 28692, Villanueva de la Cañada, Madrid, Spain*

¹⁰*X-ray Astrophysics Laboratory, NASA Goddard Space Flight Center, Greenbelt, MD 20771, USA*

¹¹*Oak Ridge Associated Universities, NASA NPP Program, Oak Ridge, TN 37831, USA*

¹²*Kavli Institute for Astronomy and Astrophysics, Peking University, Beijing 100871, China*

¹³*Department of Physics and Astronomy, Clemson University, Kinard Lab of Physics, Clemson, SC 29634, USA*

¹⁴*Department of Astronomy, University of Virginia, P.O. Box 400325, Charlottesville, VA 22904, USA*

¹⁵*Center for Astro, Particle, and Planetary Physics (CAP3), New York University Abu Dhabi, P.O. Box 129188, Abu Dhabi, UAE*

ABSTRACT

Recent models suggest approximately half of all accreting supermassive black holes (SMBHs; $M_{\text{BH}} \gtrsim 10^5 M_{\odot}$) are expected to undergo intense growth phases behind Compton-thick ($N_{\text{H}} > 1.5 \times 10^{24} \text{ cm}^{-2}$) veils of obscuring gas. However, despite being a viable source for the seeding of SMBHs, there are currently no examples known of a Compton-thick accreting intermediate mass black hole (IMBH; $M_{\text{BH}} \sim 10^2 - 10^5 M_{\odot}$). We present a detailed X-ray spectral analysis of IC 750 – the only AGN to-date with a precise megamaser-based intermediate mass $< 10^5 M_{\odot}$. We find the equivalent width of neutral 6.4 keV Fe K α to be $1.9^{+2.2}_{-1.0}$ keV via phenomenological modelling of the co-added 177 ks *Chandra* spectrum. Such large equivalent widths are seldom produced by processes other than fluorescence from dense obscuration. We fit three physically-motivated X-ray spectral models to infer a range of possible intrinsic 2–10 keV luminosity posteriors that encompass the systematic uncertainties associated with a choice of model. Despite a wide range of predicted intrinsic 2–10 keV luminosities between $\sim 10^{41}$ and $10^{43} \text{ erg s}^{-1}$, all three models agree that IC 750 has a Compton-thick line-of-sight column density to $> 99\%$ confidence. Compton-thick obscuration is well-documented to impinge substantial bias on the pursuit of SMBH AGN. Our results thus provide the first indication that Compton-thick obscuration should also be properly considered to uncover and understand the IMBH population in an unbiased manner.

Keywords: Intermediate mass black holes (86) — X-ray active galactic nuclei (2035) — X-ray astronomy (1810)

1. INTRODUCTION

It is well established that circum-nuclear obscuration and accretion rate are critical parameters that shape how supermassive black holes (SMBHs; $M_{\text{BH}} \gtrsim 10^5 M_{\odot}$) grow. The majority of radiatively-efficient active galactic nuclei (AGN) are obscured, both in the local Uni-

* NASA Postdoctoral Program Fellow

† GECO Fellow

verse (e.g., Ricci et al. 2017a; Kammoun et al. 2020; Boorman et al. 2024) and out to higher redshifts (e.g., Ueda et al. 2014; Buchner et al. 2015; Ananna et al. 2019). Furthermore, accretion rate appears to regulate circum-nuclear obscuration via feedback from radiation pressure on dusty gas (Fabian et al. 2008; Ishibashi et al. 2018) that manifests as a prevalence of highly obscured sources with Eddington ratios $\lambda_{\text{Edd}} \sim 0.01 - 0.1$, and a deficit at higher Eddington ratios (Ricci et al. 2017b; Ananna et al. 2022; Ricci et al. 2022).

Intermediate mass black holes (IMBHs; $M_{\text{BH}} \sim 10^2 - 10^5 M_{\odot}$; Greene et al. 2020) provide a vital clue to understand how seed masses grew to $\gtrsim 10^7 M_{\odot}$ within $\lesssim 700$ million years after the Big Bang, when the Universe was $\lesssim 5\%$ of its current age (e.g., Bañados et al. 2018; Goulding et al. 2023). Even though massive black holes tend to be most detectable via observable signatures of remnant or ongoing accretion activity, today very few AGN with confirmed intermediate masses are known (e.g., Greene & Ho 2007; Dong et al. 2012; Reines et al. 2013; Sartori et al. 2015; Baldassare et al. 2017; Reines 2022). Of the already-small confirmed active IMBH population, very few have robust measurements of accretion rate nor sufficiently high line-of-sight column densities that are required to understand the role that obscuration and accretion rate play in the growth of IMBHs. However, uncovering more heavily obscured IMBH AGN is a difficult challenge. Any biases imposed on selecting accreting SMBHs in heavily obscured AGN (e.g., Brandt & Alexander 2015; Ricci et al. 2015; Baloković 2017; Hickox & Alexander 2018; Torres-Albà et al. 2021) would be exacerbated in the case of accreting IMBHs which are intrinsically lower luminosity and easily confused with competing star formation-related processes.

For example, current optical spectroscopic surveys searching for accreting IMBHs require any AGN emission to exceed the competing emission from star formation in the host galaxy (e.g., Greene & Ho 2004; Moran et al. 2014). X-ray observations are less affected by host contamination and so can be a powerful tool for finding low-luminosity obscured AGN (e.g., Mezcuca et al. 2016; Annuar et al. 2017; Chen et al. 2017a; Annuar et al. 2020; Ansh et al. 2023; Mohanadas & Annuar 2023). In particular Ansh et al. (2023) present detailed broadband X-ray and multi-wavelength analysis of one of the highest obscuration dwarf AGN currently known, finding a substantial line-of-sight column density of $N_{\text{H}} = 3.4 - 7.0 \times 10^{23} \text{ cm}^{-2}$. However to-date no intermediate mass AGN have been confirmed with a

Compton-thick ($N_{\text{H}} > 1.5 \times 10^{24} \text{ cm}^{-2}$) line-of-sight column density.¹

An additional challenge arises from attaining robust black hole mass measurements. Precise and accurate mass measurements for any type of obscured massive black hole are notoriously difficult (e.g., Koss et al. 2022). One of the most accurate mass measurement techniques known arises from the Keplerian rotation of water vapour emission at 22 GHz in megamasers (Churchwell et al. 1977). Due to the requirement of nearly edge-on dense obscuration for detection, all known examples are obscured in X-rays with a substantial fraction found to be Compton-thick (e.g., Greenhill et al. 2008; Masini et al. 2016; Brightman et al. 2016, 2017). Additional complexities associated with the X-ray spectral fitting of obscured AGN can be simplified with megamasers since the line-of-sight inclination can be frozen to edge-on, removing a large source of uncertainty in physically-motivated obscuration models (e.g., Boorman et al. 2024). Despite recent advancements related to megamaser emission detections in AGN (e.g., Panessa et al. 2020), the number of sources with detected disk megamasers that are required for robust black hole mass measurements are small and almost always associated with black hole masses in the range $M_{\text{BH}} \sim 10^6 - 10^8 M_{\odot}$ (Masini et al. 2016).

Here we present the X-ray spectral analysis of IC 750 (redshift-independent distance of 14.1 Mpc; Zaw et al. 2020) – the first and currently only disk megamaser confirmed to host an IMBH. The target was identified by Chen et al. (2017a) from the 40-month *NuSTAR* serendipitous survey (Lansbury et al. 2017), in which the source was found to have 22 ± 11 counts in the hard X-ray 8–24 keV passband. Though the serendipitous detection was too faint with *NuSTAR* for informed constraints from spectral fitting, the authors reported a line-of-sight column density in excess of $\sim 10^{23} \text{ cm}^{-2}$ derived from phenomenological fitting of the archival 14 ks *Chandra* observation. By fitting Keplerian rotation curves to the 22 GHz megamaser data, Zaw et al. (2020) then constrained the central black hole mass posterior to be enclosed within $4 - 14 \times 10^4 M_{\odot}$ with a mode of $7 \times 10^4 M_{\odot}$. The considerably low black hole mass for the IC 750 deviates ~ 2 dex below standard scaling relations between black hole mass and stellar velocity dispersion and ~ 1 dex below relations with bulge mass and stellar mass (e.g., Kormendy & Ho 2013; Greene

¹ We define a Compton-thick threshold by the inverse of the Thomson optical depth, noting however that the threshold does depend on other factors such as metallicity; see <http://mytorus.com/mytorus-instructions.html> for more information.

et al. 2020). Most recently, Boorman et al. (2024) reported the co-added *Chandra* spectrum of IC 750, totalling 177 ks of effective exposure time. The updated spectral quality of the co-added X-ray spectrum indicated a large Iron K α line with an equivalent width in excess of 2 keV when fit with a simple phenomenological prescription for the underlying continuum. Such extreme fluorescence lines are currently exclusively observed in heavily Compton-thick AGN (e.g., Levenson et al. 2002; Boorman et al. 2018), strongly indicating IC 750 to be the first Compton-thick intermediate mass AGN.

The paper is organised as follows: In Section 2, we extract spectra for every epoch of *Chandra* data available for IC 750, before co-adding. We then report the results of fitting the co-added *Chandra* spectrum with three physically-motivated obscuration models in Section 3 before comparing our results with other confirmed megamasers.

2. ANALYSIS

2.1. *Chandra* Observations

The central kiloparsec of the host galaxy of IC 750 encompasses ~ 10 arcsec on the sky (see right panel of Figure 1). Since off-nuclear X-ray contaminants can have comparable observed flux to lower mass (and lower-luminosity) AGN (e.g., Brightman et al. 2018), we focus solely on *Chandra* data in this work due to its high angular resolution. Each *Chandra* observation of IC 750 was reprocessed using the Chandra Interactive Analysis of Observations (CIAO²; Fruscione et al. 2006) command `chandra_repro`.

We next used the CIAO command `fluximage` to produce exposure-corrected images and exposure maps for each observation in the broad 0.5–7 keV and narrow 6.1–6.6 keV energy bands. The latter passband was chosen to encompass observed frame FeK emission in the source. We used `reproject_obs` to reproject all observations to a new reference point, before running `flux_obs` to co-add the reprojected observations into individual exposure-corrected images. The resulting broadband and FeK images are shown in the left and centre panels of Figure 1, respectively. Although a number of off-nuclear contaminants are revealed within ~ 7 –15 arcsec of IC 750 (see Zaw et al. 2020 for more information), the AGN is clearly spatially identified by its FeK emission shown in the centre panel.

We extracted source + background counts for each observation separately from a circular region of 2 arcsec

radius centered on the source. The background counts were extracted from an annular region centered on the source with 36 arcsec and 94 arcsec inner and outer radii, respectively. The background regions were additionally chosen to exclude off-nuclear contaminants and any diffuse emission associated with the host galaxy. The source + background and background spectral files, as well as response and effective area files, were created using the CIAO command `specextract`. The co-added *Chandra* spectrum was then binned using the optimal prescription of Kaastra & Bleeker (2016) using `ftgrouppha`³.

Table 1 shows that the count rates in the soft and hard bands are all consistent across the different epochs. We note that the decreasing soft band count rate over time is fully consistent with the effective area degradation of *Chandra*. To search for any possible signs of spectral variability, we additionally fit each *Chandra* spectrum with a phenomenological prescription (see Section 3.1 for more information). We then used quantile-quantile difference plots together with posterior predictive checks (see Buchner & Boorman 2023 for more information) to test how well the spectral fits to each epoch can explain the data of each other epoch. We find no significant evidence for spectral variability between epochs, so we co-added the spectra from all six observations using the FTTOOL command `addspec`⁴. The final co-added spectrum that we use for all spectral fitting in this paper constitutes a net exposure of 177 ks with a net count rate in the 0.5–8 keV passband of 2.43 ± 0.12 counts/ks corresponding to a total of 430 net counts (see Table 1 for the observed properties of the individual and co-added spectra).

2.2. X-ray Spectral Fitting

All X-ray spectral fitting presented in this paper was performed with PYXSPEC (Gordon & Arnaud 2021), the Python implementation of the X-ray Spectral Fitting software XSPEC (Arnaud 1996). Spectral fits were carried out using the W-statistic⁵ (also known as the modified C-statistic; Wachter et al. 1979). All parameter exploration was carried out with the Bayesian X-ray Analysis software package (BXA v4.0.5; Buchner et al. 2014; Buchner 2016), which connects PYXSPEC to the nested sampling package ULTRANEST v4.0.5 (Buchner 2021). To aid the computation time associated with sampling new points of higher likelihood throughout the

² <https://cxc.cfa.harvard.edu/ciao>

³ <https://heasarc.gsfc.nasa.gov/lheasoft/help/ftgrouppha.html>

⁴ <https://heasarc.gsfc.nasa.gov/ftools/caldb/help/addspec.txt>

⁵ <https://heasarc.gsfc.nasa.gov/xanadu/xspec/manual/XSappendixStatistics.html>

Table 1. *Chandra* data used in this work.

Obs. ID (1)	PI (2)	Obs. start (3) UT	Δt (4)	T (5) ks	$\mathcal{C}_{\text{soft}}$ (6) ct / ks	$\mathcal{C}_{\text{hard}}$ (7) ct / ks	$\mathcal{C}_{\text{broad}}$ (8) ct / ks	$\mathcal{S}_{\text{soft}}$ (9)	$\mathcal{S}_{\text{hard}}$ (10)	$\mathcal{S}_{\text{broad}}$ (11)
17006	J. Darling	2014-Oct-05, 01:16	...	29.7	2.75 ± 0.31	0.82 ± 0.17	3.61 ± 0.35	10.5	5.4	11.8
22966	I. Zaw	2020-Jul-30, 10:53	+ 5.8 years	48.5	1.31 ± 0.16	0.81 ± 0.13	2.16 ± 0.21	9.1	6.8	11.4
22967	I. Zaw	2021-Feb-22, 00:56	+ 6.8 months	29.7	1.37 ± 0.22	0.91 ± 0.18	2.31 ± 0.28	7.3	5.7	9.3
24968	I. Zaw	2021-Feb-22, 16:49	+ 15.9 hours	19.7	1.06 ± 0.23	0.99 ± 0.23	2.25 ± 0.34	5.2	4.8	7.4
22603	I. Zaw	2021-Jul-25, 23:37	+ 5.0 months	24.8	1.08 ± 0.21	0.90 ± 0.19	2.02 ± 0.29	5.9	5.1	7.9
25095	I. Zaw	2021-Jul-28, 09:19	+ 2.4 days	24.8	1.20 ± 0.22	0.94 ± 0.20	2.22 ± 0.30	6.2	5.3	8.3
Co-add	177.1	1.50 ± 0.09	0.87 ± 0.07	2.43 ± 0.12	18.7	13.5	23.3

Notes. (1)–observation ID; (2)–Principle Investigator for the observation; (3)–observation start date and time; (4)–time difference relative to previous row; (5)–net exposure time in ks; (6), (7) and (8)–net count rate in counts per ks for the soft (0.5–2 keV), hard (2–8 keV) and broad (0.5–8 keV) bands, respectively; (9), (10) and (11)–signal-to-noise in the soft, hard and broad bands, respectively, computed with the `gv_significance` library of Vianello (2018).^a The factor of ~ 2 decrease in soft X-ray count rate of the later observations relative to the 2014 observation is due to the soft band degradation of *Chandra*. The soft band fluxes are comparable across all epochs.

^a https://github.com/giacomov/gv_significance

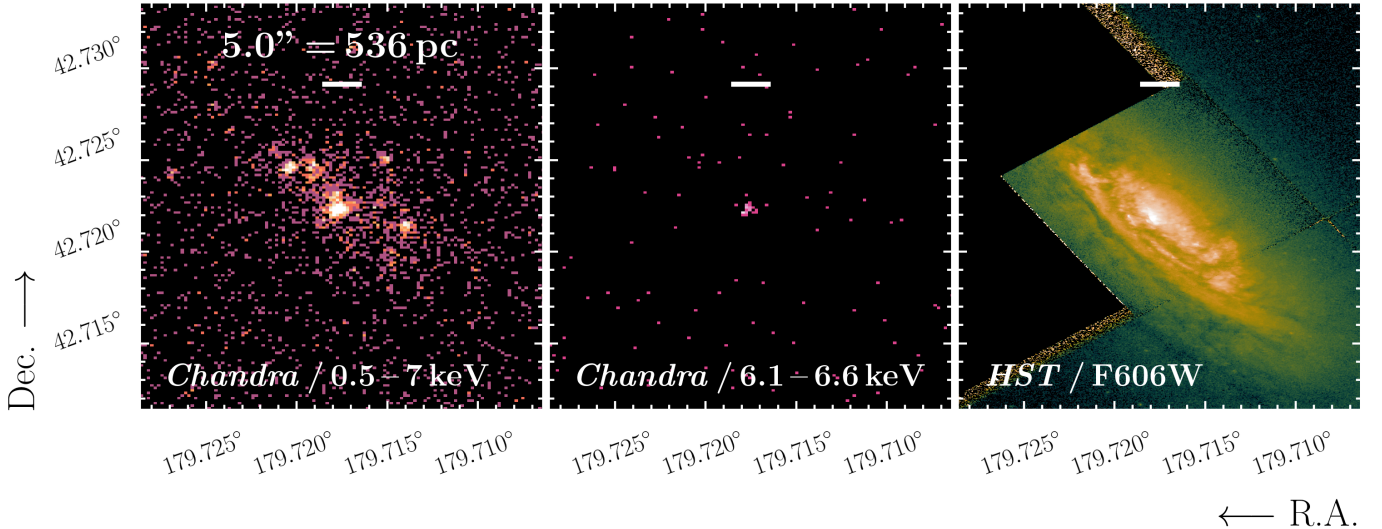


Figure 1. *Left:* Co-added 177 ks exposure *Chandra* image in the 0.5–7 keV passband. *Centre:* Co-added *Chandra* image in the 6.1–6.6 keV passband. The central AGN produces significant flux consistent with Fe K α . *Right:* Optical *HST*/F606W image centred on the nucleus of IC 750. All panels are matched in coordinates, and oriented such that north is up and east is to the left.

fitting process, we use step samplers within ULTRANEST (Buchner 2022), initially starting from a given number of steps and doubling until convergence is achieved. As recommended by Buchner (2024), we use the relative jump distance to verify our nested sampling chains have converged. Specifically, we quote the geometric mean random jump distance and the proportion of random jump distances above unity for each fit.

All spectral parameters are quoted as the maximum a posteriori value together with the 90% highest density interval integrated from each corresponding marginalised posterior mode, unless stated otherwise.

All luminosities reported for IC 750 use the distance adopted by Zaw et al. (2020) of 14.1 Mpc, which was used in the calculation of the black hole mass. The distance was estimated by Zaw et al. (2020) from the dynamics of the NGC 4111 group that IC 750 belongs to. For luminosities used from other works, we convert the luminosities to an equivalent distance of 14.1 Mpc. The photon index of the intrinsic coronal emission for all spectral fits was assigned a Gaussian prior of mean 1.8 and standard deviation 0.15 and the cut-off energy was frozen to 300 keV in all fits presented in this paper, in agreement with population studies of local AGN (e.g.,

Baloković 2017; Ricci et al. 2017a, 2018; Baloković et al. 2020). All remaining parameters were assigned uniform or log-uniform priors depending on the nature of the parameter (i.e. whether it ranges over many orders of magnitude), unless stated otherwise.

3. RESULTS & DISCUSSION

3.1. Phenomenological Fitting

As shown in the centre panel of Figure 1, there is substantial emission in the 6.1–6.6 keV energy range that is coincident with the nucleus of IC 750. This is consistent with the findings of Boorman et al. (2024) who reported an Fe K α equivalent width in excess of 2 keV derived from a simple powerlaw prescription for the underlying continuum.

To improve upon the simple prescription incorporated in that analysis, we first included the underlying reprocessed AGN continuum in a phenomenological manner. For solar abundances and typical obscurer covering factors, many X-ray radiative transfer simulations agree that the equivalent width of neutral Fe K α relative to the underlying Compton-scattered continuum is always ≥ 1 keV when the line-of-sight column density exceeds the Compton-thick threshold (Ikeda et al. 2009; Murphy & Yaqoob 2009; Brightman & Nandra 2011; Tanimoto et al. 2019). However, the underlying continuum can often comprise additional components which may saturate the total detected line flux or give rise to artificially small equivalent widths in some cases (see discussion in Levenson et al. 2002; Gandhi et al. 2017; Boorman et al. 2018 for more information).

To aid the computation time involved with fitting, we generated a custom table of the `pexrav` model (Magdziarz & Zdziarski 1995, `texrav` hereafter) to reproduce the Compton scattered continuum of IC 750. The table model was created with an appropriate spectral resolution for our *Chandra*/ACIS data, and assumes solar abundances with an edge-on inclination angle to match the megamaser in the source. Since we do not trace the peak of the Compton scattered continuum (i.e. the Compton hump at ~ 20 – 30 keV), we froze the relative normalisation of the reprocessed component to unity (Baloković 2017).

Our phenomenological model setup was constructed to follow model B2 in Section 4.2.2 of Ricci et al. (2017a). The primary X-ray coronal emission was modelled with a transmitted cut-off powerlaw. An additional cut-off powerlaw was included to reproduce a small fraction (forced to be $< 10\%$) of intrinsic emission that escapes the circum-nuclear environment through a lower column density than the primary obscurer (e.g., Gupta et al. 2021). A thermal APEC (Astrophysical Plasma Emission

Code, v.12.10.1; Smith et al. 2001) component was then used to explain any surplus of soft X-ray flux $\lesssim 3$ keV, as well as a Gaussian line to fit Iron emission between 6–7 keV at the redshift of the source. On inspection, we noticed residuals around ~ 1.8 – 1.9 keV in the individual and co-added spectra, consistent with some highly-ionised species of Silicon emission (e.g., Si XVIII). We thus included an additional Gaussian to provide a good overall fit to the entire spectrum. Liu et al. (2019) showed that polar gas is expected to produce significant Si K α emission at 1.74 keV that can be blue-shifted with respect to the host galaxy if in an outflowing configuration. However, since the line also appears strongly in the observed background (c.f. Figure 2), we adhere caution to inferring physical properties related to any tentative Silicon emission. Future high-spectral resolution observations (in particular when spatially-resolved) will enable a better understanding of low-energy outflow signatures in obscured AGN (see e.g., Matzeu et al. 2022; Gandhi et al. 2022; Barret et al. 2023).

The corresponding fit with the `texrav`-based model in folded units is shown in the upper panel of Figure 2 together with the spectral posterior ranges on the full model, Fe K α component and Silicon component. The bottom panel of Figure 2 presents the posterior cumulative difference between normalised detected counts and normalised model-predicted counts (i.e. the quantile-quantile difference; see Buchner & Boorman 2023 for more information). The green thick line and associated 90% confidence shading shows the cumulative difference of the model posterior derived from fitting the real data. We perform posterior predictive checks by simulating a large number of posterior rows with the same observational setup as the real co-added spectrum (i.e. background, response and effective area files, exposure time). The corresponding range in cumulative difference curves under the assumption that the posterior (with its associated uncertainty) were correct defines the background grey shaded region, which broadly encompasses the solid green real posterior curve. Our posterior predictive checks for the `texrav` model thus show that the model is able to reproduce the data adequately.

Figure 2 shows that the model requires significant neutral Fe K α emission, finding the rest frame line energy to be 6.40 ± 0.03 keV and observed equivalent width to be $1.9^{+2.2}_{-1.0}$ keV. Such a large equivalent width is broadly consistent with the very local Compton-thick population (see Boorman et al. 2018), though we note a large posterior uncertainty associated with the lack of underlying continuum constraints at > 10 keV. Interestingly, the fit also yields a line-of-sight column density posterior of $\log N_{\text{H}} / \text{cm}^{-2} = 24.16^{+0.83}_{-0.23}$, which is Compton-thick but

Table 2. Parameters derived from X-ray spectral fitting of IC 750.

Property	texrav	borus02	UXCLUMPY	warpeddisk	Units
$\log kT^a$	$-0.04^{+0.10}_{-0.13}$	$-0.04^{+0.16}_{-0.72}$	-0.04 ± 0.10	$-0.04^{+0.13}_{-0.19}$	keV
$\log L_{0.5-2 \text{ keV}}^b$	$38.05^{+0.17}_{-0.41}$	$37.96^{+0.29}_{-2.15}$	$38.15^{+0.05}_{-0.35}$	$38.00^{+0.17}_{-0.52}$	erg s^{-1}
Γ^c	$1.85^{+0.15}_{-0.18}$	$1.85^{+0.12}_{-0.22}$	$1.85^{+0.16}_{-0.17}$	$1.85^{+0.16}_{-0.17}$	–
$\log N_{\text{H, los}}^d$	$24.14^{+0.74}_{-0.27}$	$25.02^{+0.48}_{-0.66}$	$25.63^{+0.36}_{-1.36}$	$24.99^{+1.01}_{-0.38}$	cm^{-2}
$\log f_{\text{scat}}^e$	$0.57^{+0.43}_{-0.31}$	$-2.81^{+2.55}_{-0.36}$	$0.53^{+0.34}_{-1.01}$	$-0.71^{+0.63}_{-0.77}$	%
$\log F_{2-10 \text{ keV, obs}}^f$	$-13.46^{+0.08}_{-0.09}$	$-13.47^{+0.14}_{-0.10}$	$-13.42^{+0.07}_{-0.09}$	$-13.40^{+0.05}_{-0.10}$	$\text{erg s}^{-1} \text{ cm}^{-2}$
$\log L_{2-10 \text{ keV, obs}}^g$	$38.92^{+0.08}_{-0.09}$	$38.91^{+0.14}_{-0.10}$	$38.96^{+0.07}_{-0.09}$	$38.98^{+0.05}_{-0.10}$	erg s^{-1}
$\log L_{2-10 \text{ keV, int}}^h$	$39.87^{+0.23}_{-0.34}$	$43.25^{+0.44}_{-2.43}$	$40.96^{+0.43}_{-0.54}$	$41.55^{+0.80}_{-0.52}$	erg s^{-1}
$\log \mathcal{R}_{2-10 \text{ keV}}^i$	$1.01^{+0.19}_{-0.39}$	$4.44^{+0.44}_{-2.68}$	$2.04^{+0.36}_{-0.59}$	2.68 ± 0.65	–
$\log L_{\text{bol}}^j$	$41.22^{+0.43}_{-0.30}$	$44.63^{+0.49}_{-2.45}$	$42.42^{+0.41}_{-0.62}$	$43.00^{+0.83}_{-0.54}$	erg s^{-1}
$\log \lambda_{\text{Edd}}^k$	$-1.64^{+0.32}_{-0.44}$	$1.76^{+0.50}_{-2.32}$	$-0.58^{+0.47}_{-0.56}$	$0.07^{+0.80}_{-0.59}$	–
N_{steps}^l	1000	2000	1000	1000	–
$\overline{\text{RJD}}^m$	1.11	1.13	1.13	1.11	–
$f(\text{RJD}) > 1^n$	68.5%	69.6%	71.5%	67.7%	–
$\mathcal{Z} / \mathcal{Z}_{\text{texrav}}^o$	1	367^{+247}_{-181}	83^{+63}_{-43}	468^{+335}_{-217}	–

Notes.

Columns: (1)–physical property; (2)–parameter values derived from the phenomenological **texrav** model (note this model is least favoured – see Section 3.1); (3), (4) and (5)–parameter values derived for the **borus02**, **UXCLUMPY** and **warpeddisk** models, respectively; (6)–parameter units.

Rows: ^aTemperature of the APEC component. ^bIntrinsic luminosity of the APEC component in 0.5–2 keV. ^cPhoton index. ^dLine-of-sight column density. ^eThomson-scattered fraction. ^fObserved 2–10 keV flux. ^gObserved 2–10 keV luminosity. ^hIntrinsic 2–10 keV luminosity of the powerlaw. ⁱRatio of intrinsic-to-observed 2–10 keV flux. ^jBolometric luminosity derived with the bolometric correction of [Brightman et al. \(2017\)](#). ^kEddington ratio. ^lNumber of steps used for the step sampler within ULTRANEST. ^mThe geometric mean of the random jump distance. ⁿThe fraction of random jump distances above unity. ^oBayes Factor relative to the **texrav** model fit. We note that the positive values of all Bayes Factors indicates an improvement in the spectral fit with all models relative to **texrav**. Since the objective of this paper is not to constrain a geometry, we simply use this as a simplistic goodness-of-fit verification for our modelling.

consistent with being below the Compton-thick threshold (see Table 2 for details of other parameters in the fit).

However, the slab-based geometry assumed in **pextrav** is a poor representation of the obscuration surrounding AGN (see discussion in e.g., [Baloković 2017](#); [Paltani & Ricci 2017](#); [Buchner et al. 2021](#); [Boorman et al. 2024](#)). Furthermore, the line-of-sight column density derived is decoupled from the level of Compton scattering which can give rise to strong parameter degeneracies (e.g., between the intrinsic continuum slope and column density). Thus column densities inferred with our **texrav**-based model should be met with caution. To address this concern, we next turned to physically-motivated models with self-consistent prescriptions for photoelectric absorption, fluorescence, and Compton scattering.

3.2. *Physically-motivated Modelling*

Using different physically-motivated models⁶ on the same obscured AGN spectrum can give significantly different parameter inference (e.g., [Brightman et al. 2015](#); [LaMassa et al. 2019](#); [Saha et al. 2022](#); [Kallová et al. 2024](#); [Boorman et al. 2024](#), [Boorman et al.](#), in prep.). For this reason, we test three models described by distinct geometries: (1) **borus02** ([Baloković et al. 2018](#)) which we use in its coupled configuration to replicate a uniform

⁶ We refer to models in which photoelectric absorption, fluorescence and Compton-scattering are self-consistently modelled as physically-motivated throughout the manuscript. We note however that some models (e.g., **borus02** and **UXCLUMPY**) do not have a known physical mechanism to create and maintain their geometries, and should thus be considered ad-hoc geometries combined with X-ray radiative transfer.

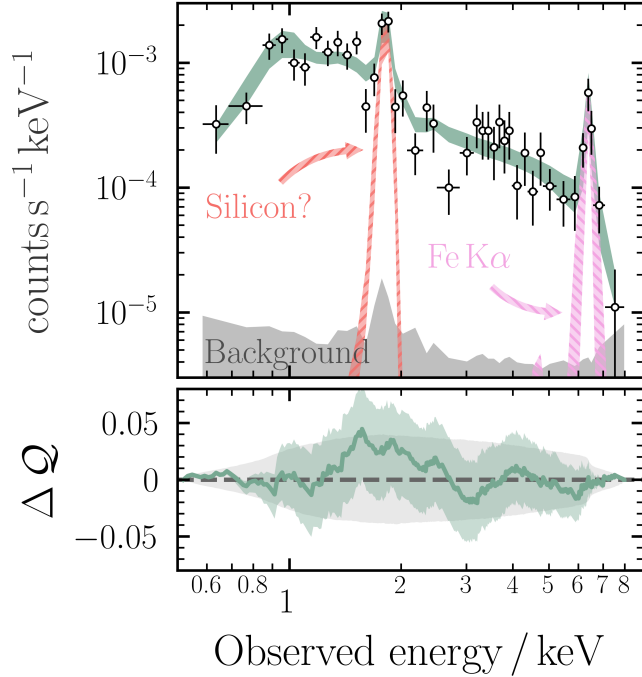


Figure 2. (Top) The co-added *Chandra* data and corresponding *texrav*-based fit, folded with the instrument response. The background has been subtracted for visual clarity, but was not subtracted during fitting. The total posterior model range is shown in green, together with the posterior constraint on the Fe K α and tentative Silicon emission lines shown in pink and red hatched shaded regions, respectively. The instrument background is plotted with grey shading at the bottom of the panel. (Bottom) Difference in the cumulative posterior model predicted counts and cumulative measured data counts are plotted as a function of energy with green shading. Simulated posterior predictive checks, showing the range expected if the derived posterior were true, is shown in grey. Since the green posterior is broadly bounded by the grey shaded region, we deem the fit as acceptable.

density sphere with parameterised polar cutouts. (2) *UXCLUMPY* (Buchner et al. 2019), a clumpy configuration of variable size gas clouds and an additional Compton-thick inner ring. (3) *warpeddisk* (Buchner et al. 2021), in which the primary obscurer arises from a Compton-thick disk with variable warp strength. The latter model holds particular physical interest since IC 750 has been found to possess a ~ 0.2 pc diameter warped maser disk (Zaw et al. 2020). For results arising from the X-ray spectral fitting with *MYtorus* (Murphy & Yaqoob 2009), see Zaw et al., in prep.

All fits fundamentally included the same components as in the phenomenological *texrav*-based fit described in Section 3.1, although the *texrav* component was replaced with the reprocessed (Compton scattered and fluorescence) spectrum and the intrinsic powerlaw was replaced with the transmitted component of each model.

The Thomson-scattered component used to reproduce the soft excess in obscured AGN was included, but for *UXCLUMPY* and *warpeddisk* this component is provided as its own table model replicating Thomson scattering from optically thin material.

Figure 3 shows the unfolded spectral posteriors for each of the three physically-motivated models. The strong Fe K α line is reproduced well by each model with somewhat similar overall contributions to the full ~ 0.5 – 8 keV passband being fit over. The quantile-quantile difference panels for each physically-motivated model fit appear to show a similar shape. The characteristic ‘S’ shape that is visible with an inflection at $\gtrsim 2$ keV is due to the apparent deficit of signal between ~ 2 – 3 keV. Such a flux deficit is somewhat reminiscent of an absorption feature, but our posterior predictive checks (grey shaded region in the lower panels of Figure 3) show that such a feature is not significant given the uncertainty associated with the observed data. It is also important to note that the *Chandra* data being fit is co-added from many different epochs, such that a flux deficit of the level shown could plausibly be a stochastic fluctuation. An interesting alternative interpretation could be that the flux deficit actually traces the underlying continuum with an additional broad emission feature between ~ 3 – 4 keV. Such emission features have received significant attention in the literature as a signature of sterile neutrino decay tracing dark matter (e.g., Bulbul et al. 2014). However, all the caveats mentioned previously (i.e. posterior predictive checks and artefacts arising from co-adding) are just as pertinent for this alternative possibility as for the presence of absorption features. Future deeper observations with *Chandra* could help discern any faint absorption or emission features in greater detail.

Figure 4 shows the corresponding posterior fits in terms of the predicted intrinsic AGN luminosity in the extrapolated 2–10 keV band vs. the predicted line-of-sight column density, both in logarithmic units. Whilst all three models unanimously predict line-of-sight column densities above the Compton-thick limit, each model reproduces a unique range in predicted intrinsic luminosities, the vast majority of which are inconsistent with one another. *borus02* has the widest range in allowable intrinsic AGN luminosities, extending up to $\sim 3 \times 10^{43}$ erg s $^{-1}$. However, given that the observed 2–10 keV luminosity of IC 750 is $\sim 8.3 \times 10^{38}$ erg s $^{-1}$, this would imply a significantly larger correction than the typical observed-to-intrinsic 2–10 keV luminosity fractions found for Compton-thick AGN of ~ 1.5 – 3 orders of magnitude (though this is also model dependent – see e.g., Boorman et al. 2024).

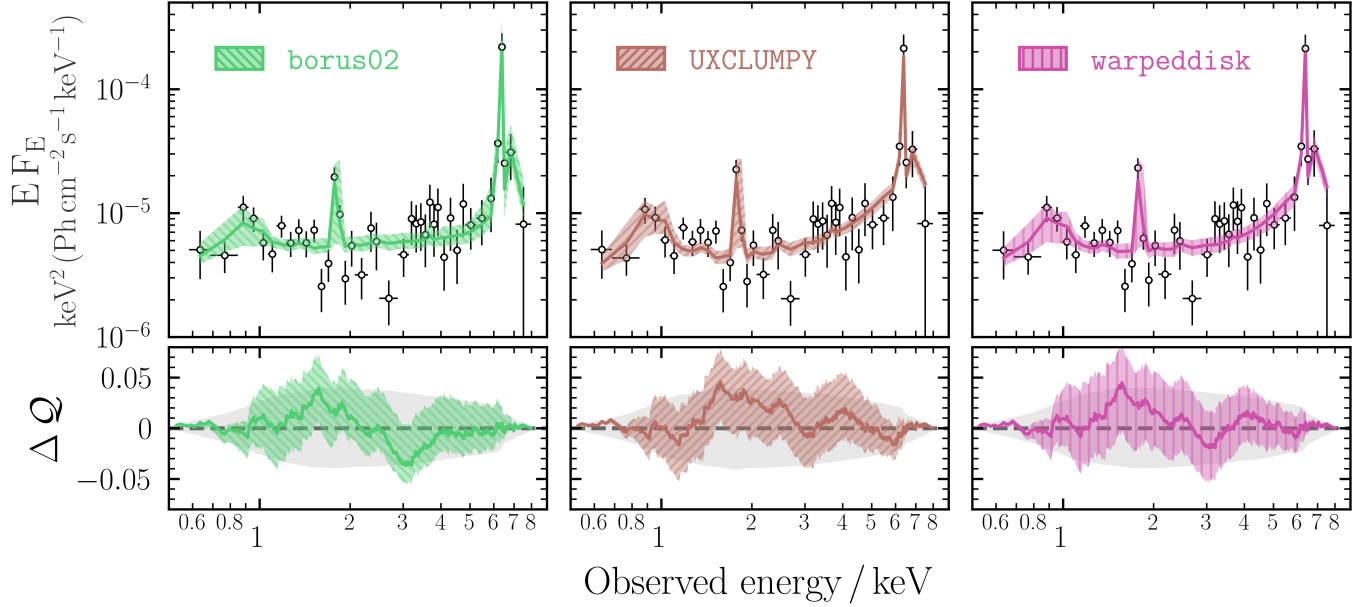


Figure 3. Unfolded spectral posteriors for each physically-motivated obscuration model fit to the co-added *Chandra* data of IC 750. Lower panels show the difference in cumulative (and normalised) model and data counts as a quantile-quantile difference plot. The grey oval-shaped regions present the 90% confidence range expected by simulating the posterior model many times with the instrumental setup of the co-added data.

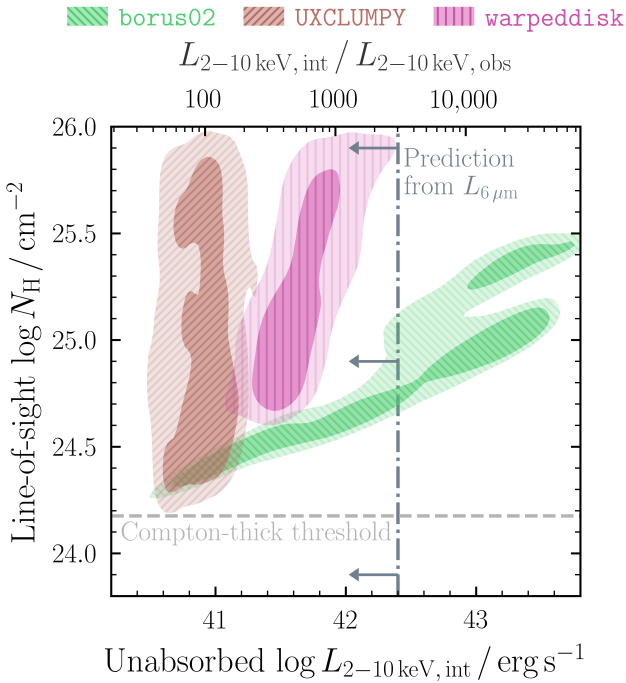


Figure 4. Two dimensional posterior contours on intrinsic 2–10 keV AGN luminosity vs. line-of-sight column density. The vertical dot-dashed line shows the upper limit on 2–10 keV luminosity predicted from the mid-infrared $6\ \mu\text{m}$ luminosity, whereas the horizontal dashed line shows the Compton-thick threshold. Though the predicted intrinsic luminosities are very discrepant amongst different models, all converge on a Compton-thick line-of-sight column density to > 99% confidence.

3.2.1. Isotropic Indicators of AGN Power

Given the relative discrepancies in predicted intrinsic luminosities of the three models being tested, it is necessary to investigate if any multi-wavelength estimators of intrinsic AGN power could potentially agree with a given model (e.g., Gandhi et al. 2014; Boorman et al. 2016; Annuar et al. 2017).

The optical [O III] line flux is known to be correlated with intrinsic AGN power when the observed line is dominated by unobstructed emission originating from the narrow line region (e.g., Panessa et al. 2006; Berney et al. 2015; Malkan et al. 2017). Zaw et al. (2020) reports a de-reddened [O III] luminosity of $\log L_{[\text{O III}]} / \text{erg s}^{-1} \sim 38.9$, which is equivalent to a predicted intrinsic X-ray luminosity of $\log L_{2-10\text{ keV}, [\text{O III}]} / \text{erg s}^{-1} \sim 40.3$ when using the best-fit to the optically-selected Seyfert 2 sample of Panessa et al. (2006). Measuring the true AGN-powered [O III] line flux is known to be uncertain due to a number of reasons including observing conditions, instrument configuration, spectral extraction method, stellar contaminating processes in the host galaxy and even the selection method by which a given sample is targeted (see discussion in Goulding & Alexander 2009; Ueda et al. 2015; Berney et al. 2015; Greenwell et al. 2021, 2022, 2024). Also, relations between the [O III] and X-ray luminosities are often calibrated for higher-mass AGN with higher metallicities that may give rise to additional scatter when inferring luminosities for lower-mass systems. All

three physically-motivated models predict intrinsic X-ray luminosities that are significantly greater than the [O III]-predicted intrinsic X-ray luminosity. One possibility is that the [O III] flux traces an earlier epoch of lower AGN activity that is causally disconnected from the more recent circum-nuclear X-ray emission detected by *Chandra*. Such ionised line emission echos are not unheard of in the local Universe (e.g., Sartori et al. 2016; Esparza-Arredondo et al. 2020; Saada et al. 2022; Pfeifle et al. 2023).

The near-to-mid infrared can be a more precise indicator of intrinsic X-ray power if the AGN-powered infrared emission can be isolated reliably (e.g., Horst et al. 2008; Gandhi et al. 2009; Asmus et al. 2014; Mateos et al. 2015; Stern 2015; Chen et al. 2017b; Pfeifle et al. 2022). Since the *Wide-field Infrared Survey Explorer (WISE)* $W1 - W2$ colour of IC 750 is ~ 0.38 mag or 0.22 mag using the instrumental profile-fit photometry or elliptical aperture magnitudes, respectively, and the source appears significantly extended in the *WISE* images, near-to-mid infrared fluxes from *WISE* are expected to be dominated by host galaxy processes (Stern et al. 2012; Assef et al. 2018; Asmus et al. 2020).

Instead, Chen et al. (2017a) present a broadband spectral energy distribution decomposition for IC 750, finding a $6\ \mu\text{m}$ luminosity of $\log L_{6\ \mu\text{m}} / \text{erg s}^{-1} \sim 42.3$ for the AGN component. A detailed look at the spectral energy distribution modelling of IC 750, following the same approach as Chen et al. (2017a) with the models of Assef et al. (2010), shows that the system is likely affected by host-obscuration beyond the level covered by the Assef et al. (2010) models. We find that re-fitting the broadband data of IC 750 by either including additional host reddening or by removing the photometry blue-ward of i -band (which is most affected by the host obscuration) results in best-fits with substantially lower AGN contributions ($\gtrsim 0.5$ dex). To be conservative, we thus adopt the $6\ \mu\text{m}$ luminosity of Chen et al. (2017a) as an upper limit.

By using the $6\ \mu\text{m}$ -to-X-ray relation for the lower-luminosity subset of Chen et al. (2017b), we derive a $6\ \mu\text{m}$ -predicted intrinsic 2–10 keV luminosity of $\log L_{2-10\ \text{keV}, 6\ \mu\text{m}} / \text{erg s}^{-1} \lesssim 42.4$ for IC 750. The predicted $6\ \mu\text{m}$ luminosity is consistent with all X-ray spectral models, but excludes the high-luminosity tail of the *borus02* model fit that would correspond to an unlikely intrinsic-to-observed 2–10 keV flux ratio of ~ 4 orders of magnitude.

3.3. Bolometric Luminosity and Eddington Ratio

Recent studies have suggested a strong link between Eddington ratio and circum-nuclear environment col-

umn density arising from the effective Eddington limit on dusty gas. The effect fundamentally predicts a minimum line-of-sight column density that can be long-lived at a given Eddington ratio (Fabian et al. 2008; Ricci et al. 2017b; Ishibashi et al. 2018). Megamasers are ideal sources to study with regard to the effective Eddington limit on dusty gas due to their high prevalence of obscuration and precise black hole mass measurements. The remaining factor that can prove difficult on a case-by-case basis is a reliable estimate of the bolometric luminosity.

We rely on the X-ray bolometric correction to estimate bolometric luminosity, $\kappa_{\text{bol}} = L_{\text{bol}} / L_{2-10\ \text{keV}}$. Whilst the bolometric correction has been extensively studied for unobscured AGN (e.g., Marconi et al. 2004; Vasudevan & Fabian 2009; Jin et al. 2012; Duras et al. 2020), it is less well-characterised for obscured AGN (e.g., Vasudevan et al. 2010; Lusso et al. 2012). Brightman et al. (2017) constrained the X-ray bolometric correction for a sample of ten local Compton-thick AGN with robust 2–10 keV intrinsic flux estimates and bolometric luminosities derived from infrared torus modelling and/or integrated spectral energy distribution modelling. The authors found an X-ray bolometric correction for the full sample of $\log \kappa_{\text{bol}} = 1.44 \pm 0.12$ (with an intrinsic scatter of ~ 0.2 dex) and no significant offset relative to bolometric corrections for less-obscured AGN. However, since our intrinsic luminosity constraints are consistent with those of the Brightman et al. (2017) sample, any bolometric correction dependence with luminosity (e.g., Marconi et al. 2004) is expected to have a minor effect. Whilst some studies report black hole mass dependence for the X-ray bolometric correction (e.g., Duras et al. (2020)), the number of AGN with precise black hole mass measurements $\lesssim 10^5$ are exceedingly low. We do note however that extrapolating the best-fit black hole mass vs. bolometric correction relation of Duras et al. (2020) gives a negligible mass dependence for IC 750.

Figure 5 presents the line-of-sight column density vs. Eddington ratio derived for IC 750 using the bolometric correction of Brightman et al. (2017), the black hole mass posterior from Zaw et al. (2020) and the posteriors found for each X-ray spectral model. We additionally plot the megamaser sample of Brightman et al. (2016) which includes Eddington ratio and line-of-sight column density estimations for 12 local Compton-thick AGN. Since Brightman et al. (2016) used a bolometric correction of 10.0, we update the Eddington ratios from that sample to use the same bolometric correction that we use for IC 750 from Brightman et al. (2017). Despite the sample of Brightman et al. (2016) having black hole masses in the range $M_{\text{BH}} \sim 10^6 - 10^8 M_{\odot}$

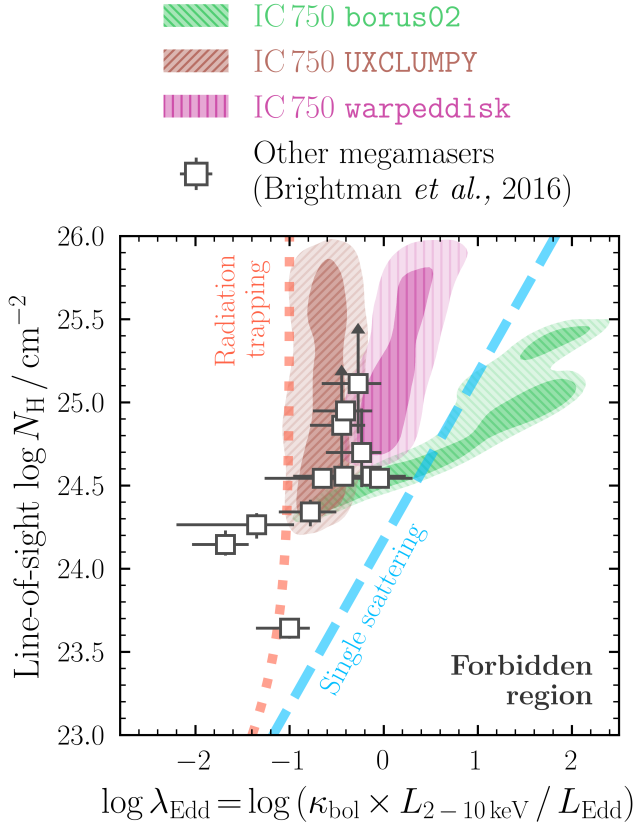


Figure 5. The Eddington ratio posteriors derived for IC 750 plotted against line-of-sight column density. The Eddington ratio posteriors were derived using the unabsorbed 2–10 keV luminosities predicted from the physically-motivated obscuration modelling whilst propagating uncertainties in black hole mass and bolometric correction. The boundaries representing the effective Eddington limits on dusty gas in the regime of radiation trapping and the single scattering UV-thin regime from Ishibashi et al. (2018) are plotted with dotted (red) and dashed (blue) lines, respectively. The sample of *NuSTAR*-studied megamaser AGN from Brightman et al. (2016) are plotted as dark grey squares with errorbars.

($\sim 1-3$ dex higher than IC 750), there is good agreement between the majority and the region of agreement for all three physically-motivated model posteriors with IC 750. The theoretical boundary arising from the single-scattering-UV assumption of Fabian et al. (2008) in which the infrared optical depth was assumed to be negligible is shown with a dashed blue line in Figure 5 and restricts the high-power tail of the *borus02* posterior, akin to the $6 \mu\text{m}$ -predicted intrinsic X-ray luminosity upper limit described in Section 3.2.1.

The second red dotted threshold in Figure 5 represents the effective Eddington limit when radiation trapping is considered in the infrared optically-thick regime (Ishibashi et al. 2018), in which a given column den-

sity can be ejected by lower Eddington ratios, even in the Compton-thick regime, than allowed by the single-scattering-UV boundary. Interestingly the vast majority of sources from Brightman et al. (2016), as well as the posteriors for IC 750, lie between the two thresholds. This could suggest that either (1) these Compton-thick AGN are actively blowing out their line-of-sight obscuration or (2) the Compton-thick megamaser AGN are in a more stable configuration in which the circumnuclear obscuration is not outflowing, and the radiation trapping threshold should lie at larger Eddington ratios for a given line-of-sight column density. Ishibashi et al. (2018) provide a number of tertiary parameters that could shift the radiation trapping boundary to lie closer to the single scattering threshold, including the dust-to-gas ratio and the clumpiness of the obscurer that can decrease the overall fraction of radiation that is trapped. Additional uncertainty arises from the different X-ray models used by Brightman et al. (2016) as compared to those fit to IC 750 in this work, as well as the sheer scarceness of Compton-thick megamaser AGN in general. The ongoing effort to search for larger samples of megamasers (e.g., Panessa et al. 2020) combined with next-generation broadband X-ray spectroscopic observations (from e.g., the *High Energy X-ray Probe*, *HEXP*; Madsen et al. 2024; Boorman et al. 2024) will enable a more complete understanding of the composition and structure of the circum-nuclear environment surrounding heavily obscured AGN across all mass scales.

3.4. Circum-nuclear Obscuration Across the Mass Scale

Bona fide intrinsically low-luminosity Compton-thick AGN with $L_{2-10\text{keV}} \lesssim 10^{41} \text{ erg s}^{-1}$ are rare, but not unheard of in the local Universe (e.g., Annuar et al. 2017; Brightman et al. 2018; da Silva et al. 2021; Boorman et al. 2024). A remaining fundamental question is thus whether IC 750 is an outlier to the existing Compton-thick AGN population or if the properties of heavily obscured AGN can naturally extend into the intermediate mass regime. Figure 6 shows the results for IC 750 relative to two populations of Compton-thick AGN identified in the literature. The left panel shows the measured equivalent width of Iron $K\alpha$ for IC 750 with the *texrav*-based model compared to the measured equivalent widths of the Compton-thick AGN population presented by Boorman et al. (2018). The right panel presents our intrinsic luminosity posterior measurements for IC 750 compared to the Database of Compton-Thick AGN (DoCTA) presented by Boorman et al. (2024) within a volume of 50 Mpc. Both the equivalent width derived with *texrav* and intrinsic luminosities covered

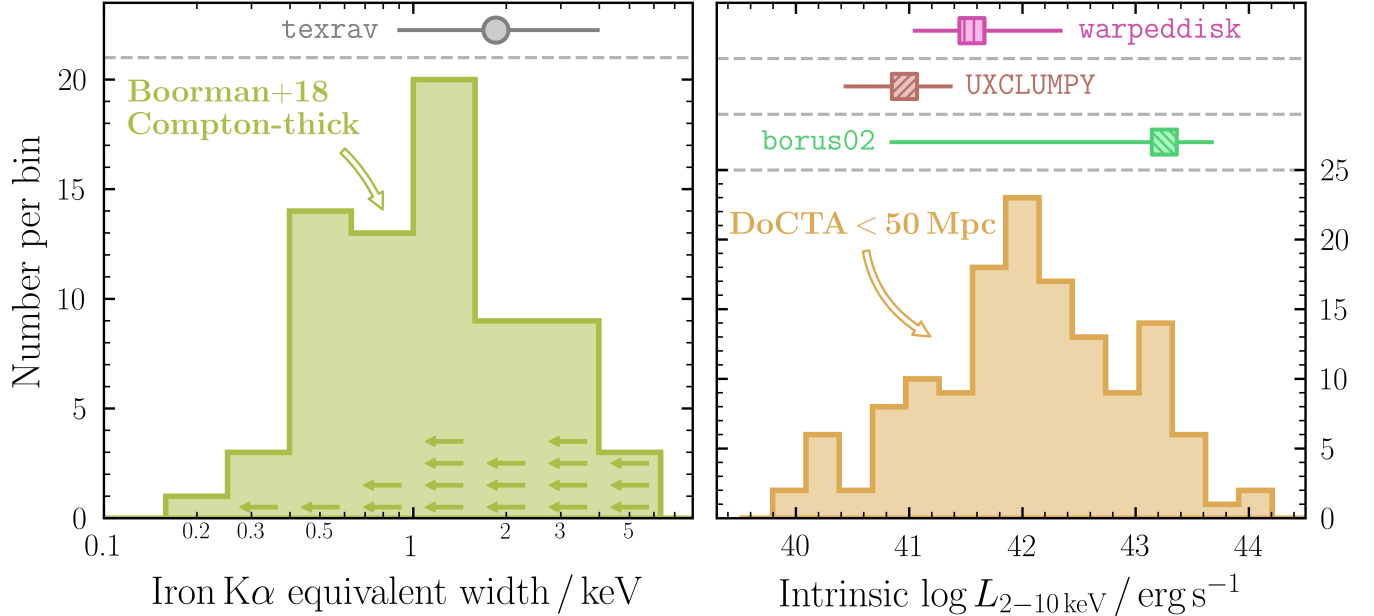


Figure 6. (Left) The distribution of Iron K α equivalent widths from the Compton-thick sample of Boorman et al. (2018) with upper limits shown as solid green arrows. The large error bar at the top of the panel shows the `texrav`-based equivalent width measurement of Iron K α for IC 750 from this work. (Right) The distribution of 295 intrinsic luminosity measurements for 30 unique Compton-thick AGN in DoCTA within $D < 50$ Mpc (Boorman et al. 2024).

by the three physically-motivated models are fully consistent with both populations, implying IC 750 shares properties with the wider Compton-thick AGN population.

4. SUMMARY AND CONCLUSIONS

We have studied the soft X-ray nuclear properties of IC 750 – the first and currently only IMBH with a megamaser-based mass measurement. Our main results are as follows:

1. By co-adding all existing *Chandra* observations for IC 750, we find a number of soft X-ray point source contaminants within ~ 7 –15 arcsec of the nucleus. However, by restricting our imaging to a narrow iron line range of 6.1–6.6 keV, we show that the vast majority of emission is coincident with the nucleus (see Section 2.1 and Figure 1). Future narrow band iron line imaging may thus prove to be a powerful technique for selecting more faint heavily obscured low mass AGN to infer properties of the underlying population. We stress that this is currently only possible with *Chandra* owing to the requirement for $\lesssim 7$ arcsec resolution imaging over the ~ 6 –7 keV passband. Future instruments with such capabilities include *HEX-P* (Madsen et al. 2024; Pfeifle et al. 2024), *AXIS* (Reynolds et al. 2023; Foord et al. 2024), *Athena* (Nandra et al. 2013; Rau et al. 2013; Meidinger et al. 2020; Barret et al. 2023) and *Lynx* (Gaskin et al. 2019).

2. By co-adding spectra extracted from each individual epoch and fitting with a phenomenological model, we find a large equivalent width of neutral Fe K α , constrained to be $1.9^{+2.2}_{-1.0}$ keV. We then fit three physically-motivated obscuration models which all find a Compton-thick line-of-sight column density to $>99\%$ probability (see Section 3 and Figures 2 and 4). This is the first confirmation of a Compton-thick IMBH.
3. The inferred intrinsic AGN power varies between the different physically-motivated models. Assuming the most up-to-date bolometric correction for Compton-thick AGN from Brightman et al. (2017), we show the source occupies Eddington ratios between ~ 0.1 –1, which exceed the effective Eddington limit for dusty gas when radiation trapping is considered (Ishibashi et al. 2018). Similar results are found for other Compton-thick megamaser AGN in the literature, suggesting that the obscuration may be outflowing or the boundary should be updated for Compton-thick column densities (see Section 3.3 and Figure 5). Approved observations with *NuSTAR* (Harrison et al. 2013) will provide vital constraints on the circum-nuclear environment and intrinsic AGN power that are not attainable with spectroscopy solely at < 8 keV. However, currently only *HEX-P* will be capable of providing well-matched simultaneous constraints

over $\sim 0.3\text{--}80$ keV for similarly faint AGN in the future (e.g., Boorman et al. 2024; Civano et al. 2024).

4. We compare our results for IC 750 to the Compton-thick Iron line equivalent width sample of Boorman et al. (2018) as well as all confirmed Compton-thick AGN from DoCTA (Boorman et al. 2024) within 50 Mpc. We find that our constraints for IC 750 are entirely consistent with the existing constraints on Iron line emission strength and intrinsic luminosity for all SMBH-powered Compton-thick AGN within this volume (see Section 3.4 and Figure 6).

One Compton-thick IMBH is insufficient to discern whether IC 750 is the tip of a hitherto unknown population or simply a single remarkable object. However, the general agreement between the existing Compton-thick AGN population and IC 750 with respect to line-of-sight column density and Eddington ratio (see Figure 5), as well as Iron $K\alpha$ equivalent width and intrinsic luminosity (see Figure 6) suggests that the presence and structure of dense circum-nuclear obscuration may be similar between accreting SMBHs and IMBHs. Dense circum-nuclear obscuration may thus prove to be an additional and necessary consideration in the pursuit of ever-increasing samples of IMBHs in the future.

ACKNOWLEDGEMENTS

We thank the anonymous referee for their constructive comments that helped to improve the manuscript. PGB would also like to thank Megan Urry, Colin Burke and Francesca Civano for useful discussions.

The work of DS was carried out at the Jet Propulsion Laboratory, California Institute of Technology, under a contract with NASA.

RJA was supported by FONDECYT grant number 1231718 and by the ANID BASAL project FB210003.

RWP gratefully acknowledges support through an appointment to the NASA Postdoctoral Program at Goddard Space Flight Center, administered by ORAU through a contract with NASA.

CR acknowledges support from Fondecyt Regular grant 1230345, ANID BASAL project FB210003 and the China-Chile joint research fund.

NTA acknowledges funding from NASA under contracts 80NSSC23K0484 and 80NSSC23K1611.

This research has made use of data obtained from the Chandra Data Archive and the Chandra Source Catalog, and software provided by the Chandra X-ray Center (CXC) in the application packages CIAO and Sherpa.

This research is based on observations made with the NASA/ESA Hubble Space Telescope obtained from the Space Telescope Science Institute, which is operated by the Association of Universities for Research in Astronomy, Inc., under NASA contract NAS 5-26555. These observations are associated with program(s)

This research has made use of the NASA/IPAC Extragalactic Database (NED), which is operated by the Jet Propulsion Laboratory, California Institute of Technology, under contract with the National Aeronautics and Space Administration.

This research has made use of NASA’s Astrophysics Data System Bibliographic Services.

This paper employs a list of Chandra datasets, obtained by the Chandra X-ray Observatory, contained in DOI:10.25574/cdc.287.

Facilities: Chandra, Hubble Space Telescope

Software: This paper made extensive use of `matplotlib` (Hunter 2007), `pandas` (pandas development team 2020; Wes McKinney 2010) and `astropy` (Astropy Collaboration et al. 2013, 2018, 2022).

REFERENCES

- Ananna, T. T., Treister, E., Urry, C. M., et al. 2019, ApJ, 871, 240, doi: [10.3847/1538-4357/aafb77](https://doi.org/10.3847/1538-4357/aafb77)
- Ananna, T. T., Urry, C. M., Ricci, C., et al. 2022, ApJL, 939, L13, doi: [10.3847/2041-8213/ac9979](https://doi.org/10.3847/2041-8213/ac9979)
- Annuar, A., Alexander, D. M., Gandhi, P., et al. 2017, ApJ, 836, 165, doi: [10.3847/1538-4357/836/2/165](https://doi.org/10.3847/1538-4357/836/2/165)
- . 2020, MNRAS, 497, 229, doi: [10.1093/mnras/staa1820](https://doi.org/10.1093/mnras/staa1820)
- Ansh, S., Chen, C.-T. J., Brandt, W. N., et al. 2023, ApJ, 942, 82, doi: [10.3847/1538-4357/ac9382](https://doi.org/10.3847/1538-4357/ac9382)
- Arnaud, K. A. 1996, in Astronomical Society of the Pacific Conference Series, Vol. 101, Astronomical Data Analysis Software and Systems V, ed. G. H. Jacoby & J. Barnes, 17
- Asmus, D., Hönig, S. F., Gandhi, P., Smette, A., & Duschl, W. J. 2014, MNRAS, 439, 1648, doi: [10.1093/mnras/stu041](https://doi.org/10.1093/mnras/stu041)
- Asmus, D., Greenwell, C. L., Gandhi, P., et al. 2020, MNRAS, 494, 1784, doi: [10.1093/mnras/staa766](https://doi.org/10.1093/mnras/staa766)
- Assef, R. J., Stern, D., Noirot, G., et al. 2018, ApJS, 234, 23, doi: [10.3847/1538-4365/aaa00a](https://doi.org/10.3847/1538-4365/aaa00a)

- Assef, R. J., Kochanek, C. S., Brodwin, M., et al. 2010, *ApJ*, 713, 970, doi: [10.1088/0004-637X/713/2/970](https://doi.org/10.1088/0004-637X/713/2/970)
- Astropy Collaboration, Robitaille, T. P., Tollerud, E. J., et al. 2013, *A&A*, 558, A33, doi: [10.1051/0004-6361/201322068](https://doi.org/10.1051/0004-6361/201322068)
- Astropy Collaboration, Price-Whelan, A. M., Sipőcz, B. M., et al. 2018, *AJ*, 156, 123, doi: [10.3847/1538-3881/aabc4f](https://doi.org/10.3847/1538-3881/aabc4f)
- Astropy Collaboration, Price-Whelan, A. M., Lim, P. L., et al. 2022, *ApJ*, 935, 167, doi: [10.3847/1538-4357/ac7c74](https://doi.org/10.3847/1538-4357/ac7c74)
- Bañados, E., Venemans, B. P., Mazzucchelli, C., et al. 2018, *Nature*, 553, 473, doi: [10.1038/nature25180](https://doi.org/10.1038/nature25180)
- Baldassare, V. F., Reines, A. E., Gallo, E., & Greene, J. E. 2017, *ApJ*, 836, 20, doi: [10.3847/1538-4357/836/1/20](https://doi.org/10.3847/1538-4357/836/1/20)
- Baloković, M. 2017, PhD thesis, California Institute of Technology
- Baloković, M., Brightman, M., Harrison, F. A., et al. 2018, *ApJ*, 854, 42, doi: [10.3847/1538-4357/aaa7eb](https://doi.org/10.3847/1538-4357/aaa7eb)
- Baloković, M., Harrison, F. A., Madejski, G., et al. 2020, *ApJ*, 905, 41, doi: [10.3847/1538-4357/abc342](https://doi.org/10.3847/1538-4357/abc342)
- Barret, D., Albouys, V., Herder, J.-W. d., et al. 2023, *Experimental Astronomy*, 55, 373, doi: [10.1007/s10686-022-09880-7](https://doi.org/10.1007/s10686-022-09880-7)
- Berney, S., Koss, M., Trakhtenbrot, B., et al. 2015, *MNRAS*, 454, 3622, doi: [10.1093/mnras/stv2181](https://doi.org/10.1093/mnras/stv2181)
- Boorman, P. G., Gandhi, P., Baloković, M., et al. 2018, *MNRAS*, 477, 3775, doi: [10.1093/mnras/sty861](https://doi.org/10.1093/mnras/sty861)
- Boorman, P. G., Gandhi, P., Alexander, D. M., et al. 2016, *ApJ*, 833, 245, doi: [10.3847/1538-4357/833/2/245](https://doi.org/10.3847/1538-4357/833/2/245)
- Boorman, P. G., Torres-Albà, N., Annuar, A., et al. 2024, *Frontiers in Astronomy and Space Sciences*, 11, 1335459, doi: [10.3389/fspas.2024.1335459](https://doi.org/10.3389/fspas.2024.1335459)
- Brandt, W. N., & Alexander, D. M. 2015, *A&A Rv*, 23, 1, doi: [10.1007/s00159-014-0081-z](https://doi.org/10.1007/s00159-014-0081-z)
- Brightman, M., & Nandra, K. 2011, *MNRAS*, 413, 1206, doi: [10.1111/j.1365-2966.2011.18207.x](https://doi.org/10.1111/j.1365-2966.2011.18207.x)
- Brightman, M., Baloković, M., Stern, D., et al. 2015, *ApJ*, 805, 41, doi: [10.1088/0004-637X/805/1/41](https://doi.org/10.1088/0004-637X/805/1/41)
- Brightman, M., Masini, A., Ballantyne, D. R., et al. 2016, *ApJ*, 826, 93, doi: [10.3847/0004-637X/826/1/93](https://doi.org/10.3847/0004-637X/826/1/93)
- Brightman, M., Baloković, M., Ballantyne, D. R., et al. 2017, *ApJ*, 844, 10, doi: [10.3847/1538-4357/aa75c9](https://doi.org/10.3847/1538-4357/aa75c9)
- Brightman, M., Baloković, M., Koss, M., et al. 2018, *ApJ*, 867, 110, doi: [10.3847/1538-4357/aae1ae](https://doi.org/10.3847/1538-4357/aae1ae)
- Buchner, J. 2016, BXA: Bayesian X-ray Analysis, Astrophysics Source Code Library, record ascl:1610.011
- . 2021, *The Journal of Open Source Software*, 6, 3001, doi: [10.21105/joss.03001](https://doi.org/10.21105/joss.03001)
- Buchner, J. 2022, in *Physical Sciences Forum*, Vol. 5, *Physical Sciences Forum*, 46, doi: [10.3390/psf2022005046](https://doi.org/10.3390/psf2022005046)
- . 2024, arXiv e-prints, arXiv:2402.11936, doi: [10.48550/arXiv.2402.11936](https://doi.org/10.48550/arXiv.2402.11936)
- Buchner, J., & Boorman, P. 2023, arXiv e-prints, arXiv:2309.05705, doi: [10.48550/arXiv.2309.05705](https://doi.org/10.48550/arXiv.2309.05705)
- Buchner, J., Brightman, M., Baloković, M., et al. 2021, *A&A*, 651, A58, doi: [10.1051/0004-6361/201834963](https://doi.org/10.1051/0004-6361/201834963)
- Buchner, J., Brightman, M., Nandra, K., Nikutta, R., & Bauer, F. E. 2019, *A&A*, 629, A16, doi: [10.1051/0004-6361/201834771](https://doi.org/10.1051/0004-6361/201834771)
- Buchner, J., Georgakakis, A., Nandra, K., et al. 2014, *A&A*, 564, A125, doi: [10.1051/0004-6361/201322971](https://doi.org/10.1051/0004-6361/201322971)
- . 2015, *ApJ*, 802, 89, doi: [10.1088/0004-637X/802/2/89](https://doi.org/10.1088/0004-637X/802/2/89)
- Bulbul, E., Markevitch, M., Foster, A., et al. 2014, *ApJ*, 789, 13, doi: [10.1088/0004-637X/789/1/13](https://doi.org/10.1088/0004-637X/789/1/13)
- Chen, C. T. J., Brandt, W. N., Reines, A. E., et al. 2017a, *ApJ*, 837, 48, doi: [10.3847/1538-4357/aa5d5b](https://doi.org/10.3847/1538-4357/aa5d5b)
- Chen, C.-T. J., Hickox, R. C., Goulding, A. D., et al. 2017b, *ApJ*, 837, 145, doi: [10.3847/1538-4357/837/2/145](https://doi.org/10.3847/1538-4357/837/2/145)
- Churchwell, E., Witzel, A., Huchtmeier, W., et al. 1977, *A&A*, 54, 969
- Civano, F., Zhao, X., Boorman, P. G., et al. 2024, *Frontiers in Astronomy and Space Sciences*, 11, 1340719, doi: [10.3389/fspas.2024.1340719](https://doi.org/10.3389/fspas.2024.1340719)
- da Silva, P., Menezes, R. B., Díaz, Y., López-Navas, E., & Steiner, J. E. 2021, *MNRAS*, 505, 223, doi: [10.1093/mnras/stab1249](https://doi.org/10.1093/mnras/stab1249)
- Dong, R., Greene, J. E., & Ho, L. C. 2012, *ApJ*, 761, 73, doi: [10.1088/0004-637X/761/1/73](https://doi.org/10.1088/0004-637X/761/1/73)
- Duras, F., Bongiorno, A., Ricci, F., et al. 2020, *A&A*, 636, A73, doi: [10.1051/0004-6361/201936817](https://doi.org/10.1051/0004-6361/201936817)
- Esparza-Arredondo, D., Osorio-Clavijo, N., González-Martín, O., et al. 2020, *ApJ*, 905, 29, doi: [10.3847/1538-4357/abc425](https://doi.org/10.3847/1538-4357/abc425)
- Fabian, A. C., Vasudevan, R. V., & Gandhi, P. 2008, *MNRAS*, 385, L43, doi: [10.1111/j.1745-3933.2008.00430.x](https://doi.org/10.1111/j.1745-3933.2008.00430.x)
- Foord, A., Cappelluti, N., Liu, T., et al. 2024, *Universe*, 10, 237, doi: [10.3390/universe10060237](https://doi.org/10.3390/universe10060237)
- Fruscione, A., McDowell, J. C., Allen, G. E., et al. 2006, in *Society of Photo-Optical Instrumentation Engineers (SPIE) Conference Series*, Vol. 6270, *Observatory Operations: Strategies, Processes, and Systems*, ed. D. R. Silva & R. E. Doxsey, 62701V, doi: [10.1117/12.671760](https://doi.org/10.1117/12.671760)
- Gandhi, P., Horst, H., Smette, A., et al. 2009, *A&A*, 502, 457, doi: [10.1051/0004-6361/200811368](https://doi.org/10.1051/0004-6361/200811368)
- Gandhi, P., Lansbury, G. B., Alexander, D. M., et al. 2014, *ApJ*, 792, 117, doi: [10.1088/0004-637X/792/2/117](https://doi.org/10.1088/0004-637X/792/2/117)
- Gandhi, P., Annuar, A., Lansbury, G. B., et al. 2017, *MNRAS*, 467, 4606, doi: [10.1093/mnras/stx357](https://doi.org/10.1093/mnras/stx357)

- Gandhi, P., Kawamuro, T., Díaz Trigo, M., et al. 2022, *Nature Astronomy*, 6, 1364, doi: [10.1038/s41550-022-01857-y](https://doi.org/10.1038/s41550-022-01857-y)
- Gaskin, J. A., Swartz, D. A., Vikhlinin, A., et al. 2019, *Journal of Astronomical Telescopes, Instruments, and Systems*, 5, 021001, doi: [10.1117/1.JATIS.5.2.021001](https://doi.org/10.1117/1.JATIS.5.2.021001)
- Gordon, C., & Arnaud, K. 2021, PyXspec: Python interface to XSPEC spectral-fitting program, *Astrophysics Source Code Library*, record ascl:2101.014
- Goulding, A. D., & Alexander, D. M. 2009, *MNRAS*, 398, 1165, doi: [10.1111/j.1365-2966.2009.15194.x](https://doi.org/10.1111/j.1365-2966.2009.15194.x)
- Goulding, A. D., Greene, J. E., Setton, D. J., et al. 2023, *ApJL*, 955, L24, doi: [10.3847/2041-8213/acf7c5](https://doi.org/10.3847/2041-8213/acf7c5)
- Greene, J. E., & Ho, L. C. 2004, *ApJ*, 610, 722, doi: [10.1086/421719](https://doi.org/10.1086/421719)
- . 2007, *ApJ*, 670, 92, doi: [10.1086/522082](https://doi.org/10.1086/522082)
- Greene, J. E., Strader, J., & Ho, L. C. 2020, *ARA&A*, 58, 257, doi: [10.1146/annurev-astro-032620-021835](https://doi.org/10.1146/annurev-astro-032620-021835)
- Greenhill, L. J., Tilak, A., & Madejski, G. 2008, *ApJL*, 686, L13, doi: [10.1086/592782](https://doi.org/10.1086/592782)
- Greenwell, C., Gandhi, P., Lansbury, G., et al. 2022, *ApJL*, 934, L34, doi: [10.3847/2041-8213/ac83a0](https://doi.org/10.3847/2041-8213/ac83a0)
- Greenwell, C., Gandhi, P., Stern, D., et al. 2021, *MNRAS*, 503, L80, doi: [10.1093/mnras/503/l80](https://doi.org/10.1093/mnras/503/l80)
- . 2024, *MNRAS*, 527, 12065, doi: [10.1093/mnras/stad3964](https://doi.org/10.1093/mnras/stad3964)
- Gupta, K. K., Ricci, C., Tortosa, A., et al. 2021, *MNRAS*, 504, 428, doi: [10.1093/mnras/stab839](https://doi.org/10.1093/mnras/stab839)
- Harrison, F. A., Craig, W. W., Christensen, F. E., et al. 2013, *ApJ*, 770, 103, doi: [10.1088/0004-637X/770/2/103](https://doi.org/10.1088/0004-637X/770/2/103)
- Hickox, R. C., & Alexander, D. M. 2018, *ARA&A*, 56, 625, doi: [10.1146/annurev-astro-081817-051803](https://doi.org/10.1146/annurev-astro-081817-051803)
- Horst, H., Gandhi, P., Smette, A., & Duschl, W. J. 2008, *A&A*, 479, 389, doi: [10.1051/0004-6361:20078548](https://doi.org/10.1051/0004-6361:20078548)
- Hunter, J. D. 2007, *Computing in Science & Engineering*, 9, 90, doi: [10.1109/MCSE.2007.55](https://doi.org/10.1109/MCSE.2007.55)
- Ikeda, S., Awaki, H., & Terashima, Y. 2009, *ApJ*, 692, 608, doi: [10.1088/0004-637X/692/1/608](https://doi.org/10.1088/0004-637X/692/1/608)
- Ishibashi, W., Fabian, A. C., Ricci, C., & Celotti, A. 2018, *MNRAS*, 479, 3335, doi: [10.1093/mnras/sty1620](https://doi.org/10.1093/mnras/sty1620)
- Jin, C., Ward, M., & Done, C. 2012, *MNRAS*, 425, 907, doi: [10.1111/j.1365-2966.2012.21272.x](https://doi.org/10.1111/j.1365-2966.2012.21272.x)
- Kaasra, J. S., & Bleeker, J. A. M. 2016, *A&A*, 587, A151, doi: [10.1051/0004-6361/201527395](https://doi.org/10.1051/0004-6361/201527395)
- Kallová, K., Boorman, P. G., & Ricci, C. 2024, *ApJ*, 966, 116, doi: [10.3847/1538-4357/ad3235](https://doi.org/10.3847/1538-4357/ad3235)
- Kammoun, E. S., Miller, J. M., Koss, M., et al. 2020, *ApJ*, 901, 161, doi: [10.3847/1538-4357/abb29f](https://doi.org/10.3847/1538-4357/abb29f)
- Kormendy, J., & Ho, L. C. 2013, *ARA&A*, 51, 511, doi: [10.1146/annurev-astro-082708-101811](https://doi.org/10.1146/annurev-astro-082708-101811)
- Koss, M. J., Trakhtenbrot, B., Ricci, C., et al. 2022, *ApJS*, 261, 1, doi: [10.3847/1538-4365/ac6c8f](https://doi.org/10.3847/1538-4365/ac6c8f)
- LaMassa, S. M., Yaqoob, T., Boorman, P. G., et al. 2019, *ApJ*, 887, 173, doi: [10.3847/1538-4357/ab552c](https://doi.org/10.3847/1538-4357/ab552c)
- Lansbury, G. B., Stern, D., Aird, J., et al. 2017, *ApJ*, 836, 99, doi: [10.3847/1538-4357/836/1/99](https://doi.org/10.3847/1538-4357/836/1/99)
- Levenson, N. A., Krolik, J. H., Życki, P. T., et al. 2002, *ApJL*, 573, L81, doi: [10.1086/342092](https://doi.org/10.1086/342092)
- Liu, J., Hönig, S. F., Ricci, C., & Paltani, S. 2019, *MNRAS*, 490, 4344, doi: [10.1093/mnras/stz2908](https://doi.org/10.1093/mnras/stz2908)
- Lusso, E., Comastri, A., Simmons, B. D., et al. 2012, *MNRAS*, 425, 623, doi: [10.1111/j.1365-2966.2012.21513.x](https://doi.org/10.1111/j.1365-2966.2012.21513.x)
- Madsen, K. K., García, J. A., Stern, D., et al. 2024, *Frontiers in Astronomy and Space Sciences*, 11, 1357834, doi: [10.3389/fspas.2024.1357834](https://doi.org/10.3389/fspas.2024.1357834)
- Magdziarz, P., & Zdziarski, A. A. 1995, *MNRAS*, 273, 837, doi: [10.1093/mnras/273.3.837](https://doi.org/10.1093/mnras/273.3.837)
- Malkan, M. A., Jensen, L. D., Rodriguez, D. R., Spinoglio, L., & Rush, B. 2017, *ApJ*, 846, 102, doi: [10.3847/1538-4357/aa8302](https://doi.org/10.3847/1538-4357/aa8302)
- Marconi, A., Risaliti, G., Gilli, R., et al. 2004, *MNRAS*, 351, 169, doi: [10.1111/j.1365-2966.2004.07765.x](https://doi.org/10.1111/j.1365-2966.2004.07765.x)
- Masini, A., Comastri, A., Baloković, M., et al. 2016, *A&A*, 589, A59, doi: [10.1051/0004-6361/201527689](https://doi.org/10.1051/0004-6361/201527689)
- Mateos, S., Carrera, F. J., Alonso-Herrero, A., et al. 2015, *MNRAS*, 449, 1422, doi: [10.1093/mnras/stv299](https://doi.org/10.1093/mnras/stv299)
- Matzeu, G. A., Lieu, M., Costa, M. T., et al. 2022, *MNRAS*, 515, 6172, doi: [10.1093/mnras/stac2155](https://doi.org/10.1093/mnras/stac2155)
- Meidinger, N., Albrecht, S., Beitle, C., et al. 2020, in *Society of Photo-Optical Instrumentation Engineers (SPIE) Conference Series*, Vol. 11444, *Space Telescopes and Instrumentation 2020: Ultraviolet to Gamma Ray*, ed. J.-W. A. den Herder, S. Nikzad, & K. Nakazawa, 114440T, doi: [10.1117/12.2560507](https://doi.org/10.1117/12.2560507)
- Mezcua, M., Civano, F., Fabbiano, G., Miyaji, T., & Marchesi, S. 2016, *ApJ*, 817, 20, doi: [10.3847/0004-637X/817/1/20](https://doi.org/10.3847/0004-637X/817/1/20)
- Mohanadas, P., & Annuar, A. 2023, *Research in Astronomy and Astrophysics*, 23, 055002, doi: [10.1088/1674-4527/acc151](https://doi.org/10.1088/1674-4527/acc151)
- Moran, E. C., Shahinyan, K., Sugarman, H. R., Vélez, D. O., & Eracleous, M. 2014, *AJ*, 148, 136, doi: [10.1088/0004-6256/148/6/136](https://doi.org/10.1088/0004-6256/148/6/136)
- Murphy, K. D., & Yaqoob, T. 2009, *MNRAS*, 397, 1549, doi: [10.1111/j.1365-2966.2009.15025.x](https://doi.org/10.1111/j.1365-2966.2009.15025.x)
- Nandra, K., Barret, D., Barcons, X., et al. 2013, *arXiv e-prints*, arXiv:1306.2307, doi: [10.48550/arXiv.1306.2307](https://doi.org/10.48550/arXiv.1306.2307)
- Paltani, S., & Ricci, C. 2017, *A&A*, 607, A31, doi: [10.1051/0004-6361/201629623](https://doi.org/10.1051/0004-6361/201629623)

- pandas development team, T. 2020, pandas-dev/pandas: Pandas, latest, Zenodo, doi: [10.5281/zenodo.3509134](https://doi.org/10.5281/zenodo.3509134)
- Panessa, F., Bassani, L., Cappi, M., et al. 2006, *A&A*, 455, 173, doi: [10.1051/0004-6361:20064894](https://doi.org/10.1051/0004-6361:20064894)
- Panessa, F., Castangia, P., Malizia, A., et al. 2020, *A&A*, 641, A162, doi: [10.1051/0004-6361/201937407](https://doi.org/10.1051/0004-6361/201937407)
- Pfeifle, R. W., Satyapal, S., Ricci, C., et al. 2023, *ApJ*, 943, 109, doi: [10.3847/1538-4357/aca7ff](https://doi.org/10.3847/1538-4357/aca7ff)
- Pfeifle, R. W., Ricci, C., Boorman, P. G., et al. 2022, *ApJS*, 261, 3, doi: [10.3847/1538-4365/ac5b65](https://doi.org/10.3847/1538-4365/ac5b65)
- Pfeifle, R. W., Boorman, P. G., Weaver, K. A., et al. 2024, *Frontiers in Astronomy and Space Sciences*, 11, 1304652, doi: [10.3389/fspas.2024.1304652](https://doi.org/10.3389/fspas.2024.1304652)
- Rau, A., Meidinger, N., Nandra, K., et al. 2013, arXiv e-prints, arXiv:1308.6785, doi: [10.48550/arXiv.1308.6785](https://doi.org/10.48550/arXiv.1308.6785)
- Reines, A. E. 2022, *Nature Astronomy*, 6, 26, doi: [10.1038/s41550-021-01556-0](https://doi.org/10.1038/s41550-021-01556-0)
- Reines, A. E., Greene, J. E., & Geha, M. 2013, *ApJ*, 775, 116, doi: [10.1088/0004-637X/775/2/116](https://doi.org/10.1088/0004-637X/775/2/116)
- Reynolds, C. S., Kara, E. A., Mushotzky, R. F., et al. 2023, in *Society of Photo-Optical Instrumentation Engineers (SPIE) Conference Series*, Vol. 12678, UV, X-Ray, and Gamma-Ray Space Instrumentation for Astronomy XXIII, ed. O. H. Siegmund & K. Hoadley, 126781E, doi: [10.1117/12.2677468](https://doi.org/10.1117/12.2677468)
- Ricci, C., Ueda, Y., Koss, M. J., et al. 2015, *ApJL*, 815, L13, doi: [10.1088/2041-8205/815/1/L13](https://doi.org/10.1088/2041-8205/815/1/L13)
- Ricci, C., Trakhtenbrot, B., Koss, M. J., et al. 2017a, *ApJS*, 233, 17, doi: [10.3847/1538-4365/aa96ad](https://doi.org/10.3847/1538-4365/aa96ad)
- . 2017b, *Nature*, 549, 488, doi: [10.1038/nature23906](https://doi.org/10.1038/nature23906)
- Ricci, C., Ho, L. C., Fabian, A. C., et al. 2018, *MNRAS*, 480, 1819, doi: [10.1093/mnras/sty1879](https://doi.org/10.1093/mnras/sty1879)
- Ricci, C., Ananna, T. T., Temple, M. J., et al. 2022, *ApJ*, 938, 67, doi: [10.3847/1538-4357/ac8e67](https://doi.org/10.3847/1538-4357/ac8e67)
- Saade, M. L., Brightman, M., Stern, D., Malkan, M. A., & García, J. A. 2022, *ApJ*, 936, 162, doi: [10.3847/1538-4357/ac88cf](https://doi.org/10.3847/1538-4357/ac88cf)
- Saha, T., Markowitz, A. G., & Buchner, J. 2022, *MNRAS*, 509, 5485, doi: [10.1093/mnras/stab3250](https://doi.org/10.1093/mnras/stab3250)
- Sartori, L. F., Schawinski, K., Treister, E., et al. 2015, *MNRAS*, 454, 3722, doi: [10.1093/mnras/stv2238](https://doi.org/10.1093/mnras/stv2238)
- Sartori, L. F., Schawinski, K., Koss, M., et al. 2016, *MNRAS*, 457, 3629, doi: [10.1093/mnras/stw230](https://doi.org/10.1093/mnras/stw230)
- Smith, R. K., Brickhouse, N. S., Liedahl, D. A., & Raymond, J. C. 2001, *ApJL*, 556, L91, doi: [10.1086/322992](https://doi.org/10.1086/322992)
- Stern, D. 2015, *ApJ*, 807, 129, doi: [10.1088/0004-637X/807/2/129](https://doi.org/10.1088/0004-637X/807/2/129)
- Stern, D., Assef, R. J., Benford, D. J., et al. 2012, *ApJ*, 753, 30, doi: [10.1088/0004-637X/753/1/30](https://doi.org/10.1088/0004-637X/753/1/30)
- Tanimoto, A., Ueda, Y., Odaka, H., et al. 2019, *ApJ*, 877, 95, doi: [10.3847/1538-4357/ab1b20](https://doi.org/10.3847/1538-4357/ab1b20)
- Torres-Albà, N., Marchesi, S., Zhao, X., et al. 2021, *ApJ*, 922, 252, doi: [10.3847/1538-4357/ac1c73](https://doi.org/10.3847/1538-4357/ac1c73)
- Ueda, Y., Akiyama, M., Hasinger, G., Miyaji, T., & Watson, M. G. 2014, *ApJ*, 786, 104, doi: [10.1088/0004-637X/786/2/104](https://doi.org/10.1088/0004-637X/786/2/104)
- Ueda, Y., Hashimoto, Y., Ichikawa, K., et al. 2015, *ApJ*, 815, 1, doi: [10.1088/0004-637X/815/1/1](https://doi.org/10.1088/0004-637X/815/1/1)
- Vasudevan, R. V., & Fabian, A. C. 2009, *MNRAS*, 392, 1124, doi: [10.1111/j.1365-2966.2008.14108.x](https://doi.org/10.1111/j.1365-2966.2008.14108.x)
- Vasudevan, R. V., Fabian, A. C., Gandhi, P., Winter, L. M., & Mushotzky, R. F. 2010, *MNRAS*, 402, 1081, doi: [10.1111/j.1365-2966.2009.15936.x](https://doi.org/10.1111/j.1365-2966.2009.15936.x)
- Vianello, G. 2018, *ApJS*, 236, 17, doi: [10.3847/1538-4365/aab780](https://doi.org/10.3847/1538-4365/aab780)
- Wachter, K., Leach, R., & Kellogg, E. 1979, *ApJ*, 230, 274, doi: [10.1086/157084](https://doi.org/10.1086/157084)
- Wes McKinney. 2010, in *Proceedings of the 9th Python in Science Conference*, ed. Stéfan van der Walt & Jarrod Millman, 56 – 61, doi: [10.25080/Majora-92bf1922-00a](https://doi.org/10.25080/Majora-92bf1922-00a)
- Zaw, I., Rosenthal, M. J., Katkov, I. Y., et al. 2020, *ApJ*, 897, 111, doi: [10.3847/1538-4357/ab9944](https://doi.org/10.3847/1538-4357/ab9944)